IEEE Access
Multidisciplinary | Rapid Review | Open Access Journal

Received April 16, 2020, accepted April 29, 2020, date of publication May 4, 2020, date of current version May 19, 2020.

Digital Object Identifier 10.1109/ACCESS.2020.2992258

A Novel 24-Slot/10-Pole Dual Three-Phase Fractional-Slot Overlapped Winding for Low Non-Working Space Harmonics and Stator Modularization

KEYI WANG AND HEYUN LIN, (Senior Member, IEEE)
School of Electrical Engineering, Southeast University, Nanjing 210096, China

Corresponding author: Heyun Lin (hyling@seu.edu.cn)

This work was supported by the Jiangsu Education Department for Postgraduate Research and Practice Innovation Program of Jiangsu Province under Grant KYCX17_0086.

ABSTRACT This paper proposes a novel 24-slot/10-pole dual three-phase (DTP) fractional-slot overlapped winding, which can simultaneously achieve the goals of low non-working space harmonics and stator modularization. Moreover, the proposed winding inherits the majority of the merits of conventional fractional-slot concentrated winding (FSCW), such as low cogging torque, low torque ripple and short end-windings. The winding configuration of the proposal is described first, and then its magnetomotive force (MMF) analysis is conducted to calculate the winding factors by using the star of slots. According to the theoretical analysis, the harmonic reduction mechanism of the proposal is expounded in depth. In addition, a specific case of a permanent magnet synchronous machine (PMSM) equipped with the proposal is analyzed and compared with two PMSMs equipped with DTP-FSCW and two-slot-pitch fractional-slot winding (TSP-FSW) respectively by finite element method (FEM) in terms of no-load back electromotive force (EMF), cogging torque, armature reaction field, on-load torque, efficiency, and fault tolerance. A prototype with the proposed winding is built and tested to verify the theoretical analysis and numerical simulations.

INDEX TERMS Fractional-slot winding, modularization, permanent magnet synchronous machine, space harmonic.

I. INTRODUCTION

Modularization is a vital concept for large permanent magnet synchronous machines (PMSMs) used for direct-drive applications due to the benefits of easy manufacturing, low-cost transportation and simple fault recovery [1], [2]. Fractional-slot concentrated winding (FSCW) is usually employed to realize stator modularization due to its non-overlapped end-winding [2], [3]. Besides, it exhibits the advantages of high power density, low torque ripple, high efficiency and fault tolerance [2]–[7]. However, PMSMs with FSCWs usually suffer from high rotor loss caused by high non-working magnetomotive force (MMF) harmonic content produced by FSCWs [8]–[11]. Research shows that low-order sub-harmonics produced by FSCWs will induce a considerable amount of rotor loss due to their long wavelength and high relative speed to the rotor. In addition to sub-harmonics, [11] highlighted the great impact of slot-harmonics on rotor loss in machines with FSCWs. As pointed out in [11], high slot-harmonic content is an important source of the rotor losses in machines with FSCWs. Excessive rotor loss will not only reduce the efficiency of a machine but also raise the PM temperature, which will degrade the PM performance and even cause demagnetization. In addition, high PM temperature will aggravate PM corrosion caused by salt spray when PM machines are used for offshore wind power generation or ship propulsion. To reduce non-working space harmonics in modular PMSMs with FSCWs, many solutions were proposed in the past decade. In general, these solutions can be classified into two categories: 1) optimizing magnetic circuits; 2) reforming winding configurations.

Regarding magnetic circuit optimization, the most direct way is to block the magnetic flux paths of low-order sub-harmonics. A novel stator structure with flux barriers in

The associate editor coordinating the review of this manuscript and approving it for publication was Canbing Li.

the stator yoke, which was proposed in [12] and [13], can significantly reduce the 1st space harmonic generated by a 12-slot/10-pole single-layer (SL) or double-layer (DL) FSCW. Flux barriers can also be placed in stator teeth. To reduce the low-order sub-harmonics in PMSMs with SL-FSCWs, a method that employs flux barriers in the stator teeth without being wound by coils was proposed in [14]. In addition to the stator, the rotor can also be structurally modified to restrain low-order sub-harmonics. It was reported that a 12-slot/10-pole interior-mounted PM (IPM) machine with a spoke-type rotor exhibits substantially less rotor loss than that with a V-type rotor with the same design specifications [15]. This difference is mainly attributed to the block effect of the spoke-arranged rear earth PMs on the 1st space harmonic. For surface-mounted PM (SPM) machines, as pointed out in [16], placing a cut (that acts as a flux barrier) in the rotor yoke at the axis of each pole can significantly suppress the space sub-harmonics. This idea can also be applied to V-type rotors. By introducing flux barriers into the rotor yoke along the d-axes, the rotor losses of the machines with V-type rotors can be effectively decreased [17]. Apart from increasing the reluctance encountered by space sub-harmonics, the damping effect can also be applied to weaken non-working space sub-harmonics. A novel structure with damping rings and void slots in the rotor yoke for rotor loss reduction was proposed in [18].

Overall, these methods of magnetic circuit improvement focus on breaking the magnetic paths of sub-harmonics (especially the 1st harmonic) to weaken them. However, they cannot reduce high-order slot-harmonics, which also produce a substantial amount of rotor loss, as previously mentioned [11].

Unlike the magnetic circuit alteration adopted by the previously mentioned techniques, the winding reformation technique aims to directly optimize the winding MMF. One type of dual n-phase FSCW, which can eliminate all non-slot MMF harmonics, was proposed in [19]. This technique only needs to reconnect the coils without changing the basic physical structure of the FSCW, which is easy to be realized structurally. However, this technique may challenge the control of the machine when the phase number n increases. Multilayer FSCW also has the ability to reduce non-working MMF harmonics [20]–[23]. The general theory and design criteria of multilayer windings were investigated in [20]. It was pointed out in [21] that the 1st MMF harmonic produced by 12-slot/10-pole fourth-layer FSCW (FL-FSCW) can be completely removed by adjusting the turn number of particular coils. The analysis of multilayer FSCW, which considers a wide range of slot/pole combinations, was conducted in [22], based on which the general design guidelines for multilayer windings were derived. Generally, the multilayer FSCW can reduce non-working harmonics without changing the control system. However, the winding factor of the working harmonic will decrease, and the insulation among the conductors within the same stator slots has to be specially enhanced due to a large number of layers. Unlike the previously mentioned solutions, a method that uses the concentrated coils with different number of conductors per coil-side in FSCW was proposed to realize the reduction in MMF sub-harmonics [24], as elaborated in the case of the 12-slot/10-pole PMSM in [25]. This method can almost eliminate the 1st harmonic in 12-slot/10-pole FSCW without loss of the working harmonic.

Taking a general view of the winding reformation techniques above, it can be found they can only reduce the sub-harmonic content, while the slot-harmonic content remains high, which limits the reduction in rotor loss [11]. The fact that the number of slots is close to the number of poles in PMSMs with FSCWs should be responsible for this stubborn problem. Although single-layer integral-slot distributed winding (SL-ISDW) with 1 slot per pole per phase can be reconnected to achieve stator modularization [26], it has inevitable common drawbacks of ISDW, namely, high torque ripple, high cogging torque and long end-winding length.

Therefore, by increasing the number of slots based on the FSCW, the two-slot-pitch (TSP) winding was proposed to reduce the non-working slot-harmonic content. The concept of stator shifting was extensively employed to form the TSP winding. The comprehensive description and analysis of stator shifting were presented in [27]. A novel 24-slot/10-pole TSP winding that is composed of two shifted 12-slot/10-pole FSCWs with different coil turns, which can simultaneously reduce sub-harmonic content and slot-harmonic content, was proposed in [28]. [29] proposed another type of TSP winding by connecting two conventional FSCWs shifted by 180 mechanical degrees, which exhibits substantially lower non-working harmonic content than FSCW. [30] optimized the shifting angle of this type of winding to form a six-phase 18-slot/10-pole TSP winding, which further reduces non-working harmonic content. [31] presented feasible slot/pole combinations and the general theory of machines with TSP windings. [32] applied the method of stator shifting to 12-slot/10-pole dual three-phase (DTP) FSCW to form a six-phase 24-slot/10-pole TSP winding, which not only eliminates sub-harmonics but also significantly reduces non-working slot-harmonics. [33] made a comparison between two IPM machines with 12-slot/10-pole FSCW and 24-slot/10-pole TSP winding, which shows the advantage of TSP winding in low rotor loss. [34] discussed two ways of phase belt arrangement for six-phase TSP windings. In [35], the sub-harmonics existing in TSP windings can be further reduced by altering the turn numbers of some coils. To remove more non-working harmonics without excessive loss of the working harmonic, [36] further improved TSP winding using coils with different number of turns. This improved TSP winding was successfully applied in 18-slot/10-pole and 24-slot/10-pole machines.

The research above show that the TSP winding exhibits much lower non-working slot-harmonic content than the FSCW. However, all the TSP winding configurations presented above lose the advantage of stator modularization because they exhibit continuous overlapped end-windings

that cover the ends of the ends of the stator. Thus, they cannot be adopted to build modular machines.

To solve the incompatibility between low non-working space harmonics and stator modularization, this paper proposes a novel 24-slot/10-pole (as a cell machine) DTP fractional-slot overlapped winding to simultaneously achieve low space harmonic content and stator modularization while retaining most of the advantages of the conventional FSCW. First, the configuration of the novel winding is described in detail. Second, the MMF and the winding factors of the proposal are computed to explain the harmonic reduction mechanism. A PMSM equipped with the proposed winding is analyzed and compared with two PMSMs with DTP-FSCW and two-slot-pitch fractional-slot winding (TSP-FSW) by finite element method (FEM). Last, a prototype with the proposed winding is fabricated and measured to verify the theoretical analysis and numerical simulations.

II. WINDING CONFIGURATION

The configuration of the proposed winding is illustrated in Fig. 1. Fig.1 (a) shows that the proposed winding is a DTP winding, which can be structurally regarded as a combination of two sets of symmetrical three-phase windings (referred to as winding-I and winding-II). It is obvious that winding-I (A_1, B_1 and C_1) is a DL-winding, while winding-II (A_2, B_2 and C_2) is a SL-winding and they are overlapped. Hence, the proposed winding is a *mixed-layer* winding, which means that some stator slots contain two coil-sides, while other stator slots only contain one coil-side.

Regarding the structural details, it should be noted that two different types of TSP coils are employed in the proposed winding: one is the special coil with unequal conductor number per coil-side (referred to as UCNC), and the other is the conventional coils with equal conductor number per coil-side (referred to as ECNC). Winding-I consists of UCNCs and winding-II consists of ECNCs. The coil-side conductor numbers of UCNC and ECNC are denoted by N_1, N_2 and N_3, as indicated in Fig. 1 (a). To realize UCNC, the in-turn and the out-turn of a UCNC are arranged to be located on the same coil-side, which means that they are contained in the same stator slot. Thus, the difference between the numbers of conductors in the two coil-sides of a UCNC must be one, as pointed out in [24] and [25]. Fig. 1 (b) shows the 3D structural sketch of a UCNC, which contains two coil-sides with three and two conductors, respectively.

Totally, the proposed winding contains twelve UCNCs and six ECNCs. Each ECNC overlaps two adjacent UCNCs by half of the coil pitch (one slot), while the UCNCs do not overlap each other, and nor do the ECNCs. Thus, the stator can be segmented into six identical modules by cutting the stator along the axes of the slots without being covered by end-windings, as marked by the dashed lines in Fig. 1 (a). The single stator module is illustrated in Fig. 1 (c). As shown in Fig. 1 (c), each stator module contains one ECNC and two UCNCs.

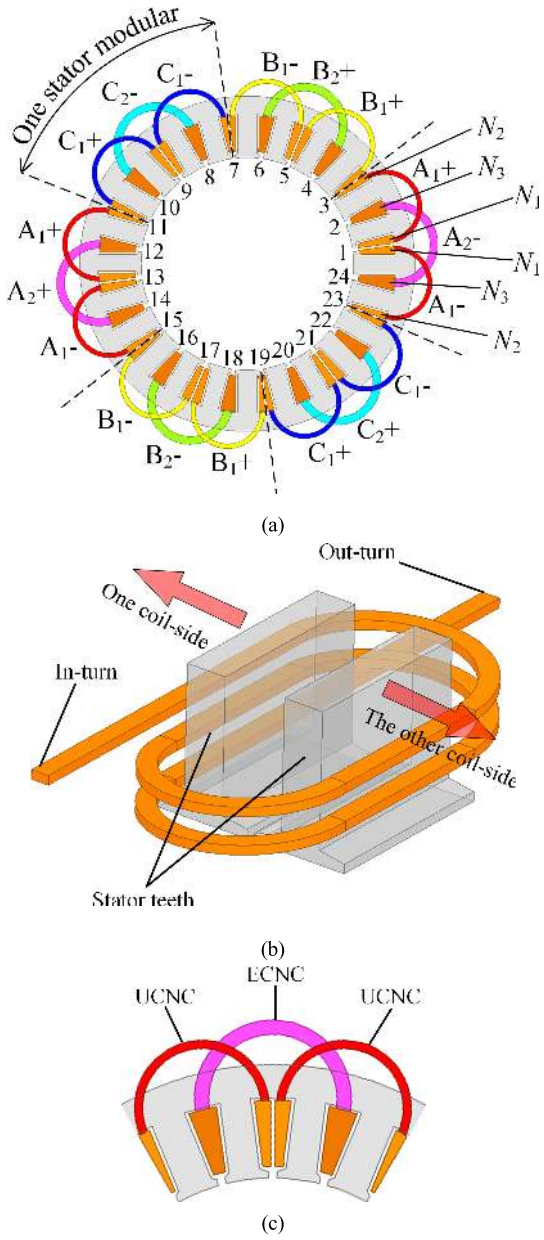

FIGURE 1. Configuration of the proposed winding. (a) Complete stator with the proposed winding. (b) 3D structural sketch of a UCNC with three conductors on one coil-side and two conductors on another coil-side. (c) Single stator module.

It is necessary to point out that the selection of the number of coil-side conductors of UCNC and ECNC (N_1, N_2 and N_3) has a great influence on the MMF and winding factors of the proposed winding, which will be investigated in detail in Section III.

III. MMF ANALYSIS AND WINDING FACTOR CALCULATION

The aim of this section is to compute the resultant MMF and winding factors of the proposed winding. First, the specific MMF functions of winding-I and winding-II are derived separately. Afterwards, the resultant MMF is obtained by superimposing these two MMF functions.

The star of slots is employed to obtain the MMFs and winding factors of the winding. The stator slots are numbered sequentially as shown in Fig. 1 (a), and the corresponding vectors are denoted by $\boldsymbol{V}_1$, $\boldsymbol{V}_2$, $\boldsymbol{V}_3$, etc. It should be emphasized that each slot vector in this paper represents the MMF space vector of the *coil-side* embedded in the corresponding stator slot rather than the whole coil because of the adoption of UCNCs.

A. WINDING-I

Assume that the three-phase currents fed in winding-I are

$$\begin{aligned} i_{\mathrm{A1}} &= I_{\mathrm{I}} \sin(2\pi ft) \\ i_{\mathrm{B1}} &= I_{\mathrm{I}} \sin\left(2\pi ft - \frac{2\pi}{3}\right) \\ i_{\mathrm{C1}} &= I_{\mathrm{I}} \sin\left(2\pi ft - \frac{4\pi}{3}\right) \end{aligned} \tag{1}$$

where I_{I} denotes the amplitude of the currents fed in winding-I, and f denotes the current frequency. The phase angle of $\boldsymbol{V}_1$ is set to zero. The slot vectors belonging to phase A_1 and their specific information are tabulated in Table 1. The vector angles in Table 1 are calculated by considering the cases of different harmonics and the winding directions of the coils.

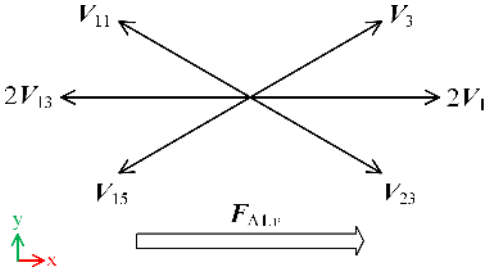

FIGURE 2. Star of slots of phase A_1.

According to Table 1, the star of slots of phase A_1 can be obtained, as illustrated in Fig. 2. It has to be clarified that Fig. 2 is only a sketch. The specific configuration in the case of a certain harmonic should strictly follow the vector information presented in Table 1.

Obviously, the ν^{th} harmonic component of the MMF space vector of phase A_1 is exactly the sum of all the vectors in Fig. 2, which can be written as

$$\boldsymbol{F}_{\mathrm{A1}.\nu} = \boldsymbol{V}_1 + \boldsymbol{V}_{13} + \boldsymbol{V}_3 + \boldsymbol{V}_{23} + \boldsymbol{V}_{11} + \boldsymbol{V}_{15} \tag{2}$$

In order to derive the specific expressions of the MMF of winding-I, two important features of Fig. 2 need to be noticed:

1) *$\boldsymbol{V}_1$ and $\boldsymbol{V}_{13}$ are always collinear along the x-axis.*

According to Table 1, both the angles of $\boldsymbol{V}_1$ and $\boldsymbol{V}_{13}$ are multiples of π, which verifies this conclusion.

2) *$\boldsymbol{V}_3$ and $\boldsymbol{V}_{23}$ ($\boldsymbol{V}_{11}$ and $\boldsymbol{V}_{15}$) are always symmetrically distributed on the two sides of the x-axis.*

The angle of the axis of symmetry of $\boldsymbol{V}_3$ and $\boldsymbol{V}_{23}$ ($\boldsymbol{V}_{11}$ and $\boldsymbol{V}_{15}$) can be obtained as

$$\frac{\angle \boldsymbol{V}_3 + \angle \boldsymbol{V}_{23}}{2} = \pi\nu + \pi, \qquad \frac{\angle \boldsymbol{V}_{11} + \angle \boldsymbol{V}_{15}}{2} = \pi\nu,$$

TABLE 1. Slot vectors belonging to phase A_1.

Vector	Modulus (A)	Angle (radian)
$\boldsymbol{V}_1$	$\frac{i_{\mathrm{A1}}N_1}{\pi\nu}$	0
$\boldsymbol{V}_{13}$	$\frac{i_{\mathrm{A1}}N_1}{\pi\nu}$	$\pi\nu+\pi$
$\boldsymbol{V}_3$	$\frac{i_{\mathrm{A1}}N_2}{\pi\nu}$	$\frac{\pi}{6}\nu+\pi$
$\boldsymbol{V}_{23}$	$\frac{i_{\mathrm{A1}}N_2}{\pi\nu}$	$\frac{11\pi}{6}\nu+\pi$
$\boldsymbol{V}_{11}$	$\frac{i_{\mathrm{A1}}N_2}{\pi\nu}$	$\frac{5\pi}{6}\nu$
$\boldsymbol{V}_{15}$	$\frac{i_{\mathrm{A1}}N_2}{\pi\nu}$	$\frac{7\pi}{6}\nu$

*ν denotes the harmonic order.

which means that the x-axis is exactly the axis of symmetry. Naturally, the correctness of the conclusion is verified.

Based on the two features above, it can be concluded that $\boldsymbol{F}_{\mathrm{A1}.\nu}$ and x-axis are always collinear as shown in Fig. 2. That is to say, the instantaneous modulus of $\boldsymbol{F}_{\mathrm{A1}.\nu}$ can be calculated by obtaining its component in the x-axis direction as follows.

$$\begin{aligned} F^{\mathrm{x}}_{\mathrm{A1}.\nu} &= \boldsymbol{F}_{\mathrm{A1}.\nu} \cdot \boldsymbol{e}_{\mathrm{x}} \\ &= \frac{2i_{\mathrm{A1}}N_1}{\pi\nu}\cos(\angle \boldsymbol{V}_1) + \frac{2i_{\mathrm{A1}}N_1}{\pi\nu}\cos(\angle \boldsymbol{V}_{13}) \\ &\quad + \frac{2i_{\mathrm{A1}}N_2}{\pi\nu}\cos(\angle \boldsymbol{V}_3) + \frac{2i_{\mathrm{A1}}N_2}{\pi\nu}\cos(\angle \boldsymbol{V}_{11}) \\ &= \frac{2I_{\mathrm{I}}}{\pi\nu}\left[N_1 - N_1\cos(\pi\nu) - N_2\cos\left(\frac{\pi}{6}\nu\right)\right. \\ &\quad \left. + N_2\cos\left(\frac{5\pi}{6}\nu\right)\right]\sin(2\pi ft) \\ &= F^{\mathrm{I}}_{\Phi.\nu}\sin(2\pi ft) \end{aligned} \tag{3}$$

where $\boldsymbol{e}_{\mathrm{x}}$ denotes the unit vector in the x-axis direction. Equation (3) shows that the MMF generated by phase A_1 is a standing wave, where $F^{\mathrm{I}}_{\Phi.\nu}$ is introduced to denote its amplitude. Thus, the MMF function of phase A_1 along the circumference of the air-gap can be obtained as

$$\begin{aligned} F_{\mathrm{A1}.\nu} &= F^{\mathrm{x}}_{\mathrm{A1}.\nu}\cos(\nu x) \\ &= F^{\mathrm{I}}_{\Phi.\nu}\sin(2\pi ft)\cos(\nu x) \quad x \in [0, 2\pi] \end{aligned} \tag{4}$$

where x denotes the coordinate value along the air-gap. Based on the deduced MMF function of phase A_1, the winding factors of winding-I can be easily calculated as

$$\begin{aligned} k^{\mathrm{I}}_{\mathrm{w}.\nu} &= \frac{\left|F^{\mathrm{x}}_{\mathrm{A1}.\nu}\right|}{\frac{2i_{\mathrm{A1}}}{\pi\nu}(2N_1 + 2N_2)} \\ &= \frac{\left|N_1\left[1-\cos(\pi\nu)\right] + N_2\left[\cos\left(\frac{5\pi}{6}\nu\right) - \cos\left(\frac{\pi}{6}\nu\right)\right]\right|}{2(N_1 + N_2)} \end{aligned} \tag{5}$$

In accordance with the spatial and the temporal relations among phases A_1, B_1 and C_1, the MMF functions of phases

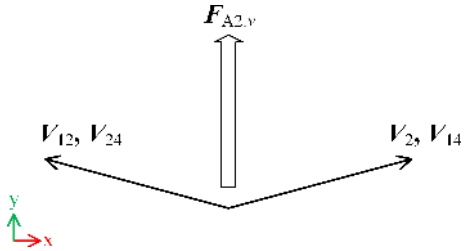

FIGURE 3. Star of slots of phase A_2.

B_1 and C_1 can be achieved directly based on (4) as

$$F_{B1.\nu} = F^{I}_{\Phi.\nu} \sin\left(2\pi ft - \frac{2}{3}\pi\right) \cos\left(\nu x - \frac{4\pi}{3}\nu\right) \quad (6)$$

$$F_{C1.\nu} = F^{I}_{\Phi.\nu} \sin\left(2\pi ft - \frac{4}{3}\pi\right) \cos\left(\nu x - \frac{8\pi}{3}\nu\right) \quad (7)$$

The MMF produced by winding-I can be obtained by summing (4), (6) and (7) as

$$\begin{aligned} F_{I.\nu} &= F_{A1.\nu} + F_{B1.\nu} + F_{C1.\nu} \\ &= \begin{cases} \frac{3}{2}F^{I}_{\Phi.\nu} \sin(2\pi ft - \nu x) & \nu = 3k+2 \\ \frac{3}{2}F^{I}_{\Phi.\nu} \sin(2\pi ft + \nu x) & \nu = 3k+1 \\ 0 & \nu = 3k \end{cases} \quad (k \in N) \end{aligned} \quad (8)$$

B. WINDING-II

The MMF analysis process of winding-II is similar to that of winding-I. Assume that the currents fed in winding-II are

$$\begin{aligned} i_{A2} &= I_{II} \sin(2\pi ft - \varphi) \\ i_{B2} &= I_{II} \sin\left(2\pi ft - \frac{2\pi}{3} - \varphi\right) \\ i_{C2} &= I_{II} \sin\left(2\pi ft - \frac{4\pi}{3} - \varphi\right) \end{aligned} \quad (9)$$

where I_{II} denotes the amplitude of the currents fed in winding-II, and φ denotes the current phase difference between winding-I and winding-II. The slot vectors of phase A_2 are tabulated in Table 2, and the corresponding star of slots is shown in Fig. 3. Thus, the MMF space vector of phase A_2 can be expressed as

$$\boldsymbol{F}_{A2.\nu} = \boldsymbol{V}_2 + \boldsymbol{V}_{24} + \boldsymbol{V}_{12} + \boldsymbol{V}_{14} \quad (10)$$

The configuration of the star of slots for phase A_2 also has two regularities:

1) *$\boldsymbol{V}_2$ and $\boldsymbol{V}_{14}$ ($\boldsymbol{V}_{12}$ and $\boldsymbol{V}_{24}$) are always collinear.*

This conclusion can be verified by calculating the difference between the angles of $\boldsymbol{V}_2$ and $\boldsymbol{V}_{14}$ ($\boldsymbol{V}_{12}$ and $\boldsymbol{V}_{24}$) as

$$\angle\boldsymbol{V}_2 - \angle\boldsymbol{V}_{14} = -\pi\nu, \quad \angle\boldsymbol{V}_{12} - \angle\boldsymbol{V}_{24} = \pi(\nu+1),$$

which shows the correctness of the conclusion.

2) *$\boldsymbol{V}_2$ and $\boldsymbol{V}_{24}$ ($\boldsymbol{V}_{14}$ and $\boldsymbol{V}_{12}$) are always symmetrically distributed on the two sides of the y-axis.*

TABLE 2. Slot vectors belonging to phase A_2.

Vector	Modulus (A)	Angle (radian)
$\boldsymbol{V}_2$	$\frac{i_{A2}N_3}{\pi\nu}$	$\frac{\pi}{12}\nu$
$\boldsymbol{V}_{24}$	$\frac{i_{A2}N_3}{\pi\nu}$	$\frac{23\pi}{12}\nu+\pi$
$\boldsymbol{V}_{12}$	$\frac{i_{A2}N_3}{\pi\nu}$	$\frac{11\pi}{12}\nu$
$\boldsymbol{V}_{14}$	$\frac{i_{A2}N_3}{\pi\nu}$	$\frac{13\pi}{12}\nu+\pi$

According to Table 2, the angle of the axis of symmetry of $\boldsymbol{V}_2$ and $\boldsymbol{V}_{24}$ ($\boldsymbol{V}_{14}$ and $\boldsymbol{V}_{12}$) is

$$\frac{\angle\boldsymbol{V}_2 + \angle\boldsymbol{V}_{24}}{2} = \frac{\pi}{2} + \pi\nu, \quad \frac{\angle\boldsymbol{V}_{14} + \angle\boldsymbol{V}_{12}}{2} = \frac{\pi}{2} + \pi\nu$$

It means that the y-axis is exactly the axis of symmetry of $\boldsymbol{V}_2$ and $\boldsymbol{V}_{24}$ ($\boldsymbol{V}_{14}$ and $\boldsymbol{V}_{12}$), which verifies the conclusion.

The two regularities above imply that $\boldsymbol{F}_{A2.\nu}$ and the y-axis are always collinear. Hence, the instantaneous modulus of $\boldsymbol{F}_{A2.\nu}$ can be obtained by obtaining its component in the y-axis direction as

$$\begin{aligned} F^{y}_{A2.\nu} &= \boldsymbol{F}_{A2.\nu} \cdot \boldsymbol{e}_y \\ &= 2\frac{i_{A2}N_3}{\pi\nu} \sin(\angle\boldsymbol{V}_2) + 2\frac{i_{A2}N_3}{\pi\nu} \sin(\angle\boldsymbol{V}_{12}) \\ &= \frac{2I_{II}N_3}{\pi\nu}\left[\sin\left(\frac{\pi}{12}\nu\right) + \sin\left(\frac{11\pi}{12}\nu\right)\right] \sin(2\pi ft - \varphi) \\ &= F^{II}_{\Phi.\nu} \sin(2\pi ft - \varphi) \end{aligned} \quad (11)$$

where $\boldsymbol{e}_y$ denotes the unit vector in the y-axis direction, and $F^{II}_{\Phi.\nu}$ denotes the amplitude of $F^{y}_{A2.\nu}$. Summarizing the above analysis, the MMF function of phase A_2 can be achieved as

$$\begin{aligned} F_{A2.\nu} &= F^{y}_{A2.\nu} \cos\left(\nu x - \frac{\pi}{2}\right) \\ &= F^{II}_{\Phi.\nu} \sin(2\pi ft - \varphi) \cos\left(\nu x - \frac{\pi}{2}\right) \quad x \in [0, 2\pi] \end{aligned} \quad (12)$$

Naturally, the winding factors of winding-II can be calculated by

$$k^{II}_{w.\nu} = \frac{1}{2}\left|\left[\sin\left(\frac{\pi}{12}\nu\right) + \sin\left(\frac{11\pi}{12}\nu\right)\right]\right| \quad (13)$$

Referring to (12), the MMF functions of phases B_2, and C_2 can be obtained instantly as

$$F_{B2.\nu} = F^{II}_{\Phi.\nu} \sin\left(2\pi ft - \frac{2}{3}\pi - \varphi\right) \cos\left(\nu x - \frac{\pi}{2} - \frac{4\pi}{3}\nu\right) \quad (14)$$

$$F_{C2.\nu} = F^{II}_{\Phi.\nu} \sin\left(2\pi ft - \frac{4}{3}\pi - \varphi\right) \cos\left(\nu x - \frac{\pi}{2} - \frac{8\pi}{3}\nu\right) \quad (15)$$

Thus, the MMF function of winding-II, which can be achieved by summing (12), (14) and (15), is presented as

$$F_{\mathrm{II}.\nu}=\begin{cases}\dfrac{3}{2}F^{\mathrm{II}}_{\Phi.\nu}\sin\left(2\pi ft-\nu x+\dfrac{\pi}{2}-\varphi\right) & \nu=3k+2\\ \dfrac{3}{2}F^{\mathrm{II}}_{\Phi.\nu}\sin\left(2\pi ft+\nu x-\dfrac{\pi}{2}-\varphi\right) & \nu=3k+1\\ 0 & \nu=3k\end{cases}\tag{16}$$

C. ENTIRE WINDING

Since the MMF functions of winding-I and winding-II have been derived, the resultant MMF produced by the entire winding can be easily obtained by adding them. In order to promote the power density as much as possible, $F_{\mathrm{I}.5}$ and $F_{\mathrm{II}.5}$ should be designed as being in phase. According to (8) and (16), the value of φ should be determined as

$$\varphi=\frac{\pi}{2}\tag{17}$$

Therefore, the resultant MMF can be simplified into

$$\begin{aligned}F_{\sigma.\nu}&=F_{\mathrm{I}.\nu}+F_{\mathrm{II}.\nu}\\&=\begin{cases}\dfrac{3}{2}\left(F^{\mathrm{I}}_{\Phi.\nu}+F^{\mathrm{II}}_{\Phi.\nu}\right)\sin\left(2\pi ft-\nu x\right) & \nu=3k+2\\ \dfrac{3}{2}\left(F^{\mathrm{I}}_{\Phi.\nu}-F^{\mathrm{II}}_{\Phi.\nu}\right)\sin\left(2\pi ft+\nu x\right) & \nu=3k+1\\ 0 & \nu=3k\end{cases}\end{aligned}\tag{18}$$

To characterize the utilization rate of all the phase currents in forming the resultant MMF, the *Resultant MMF Coefficient* (RMC) is introduced. The RMC is defined as the ratio of the amplitude of $F_{\sigma.\nu}$ to the algebraic sum of the MMFs of all the conductors. Thus, the RMC of the proposed winding is calculated as

$$k^{\sigma}_{\mathrm{MMF}.\nu}=\begin{cases}\left|\dfrac{\pi\nu\left(F^{\mathrm{I}}_{\Phi.\nu}+F^{\mathrm{II}}_{\Phi.\nu}\right)}{4\left(I_1N_1+I_1N_2+I_{\mathrm{II}}N_3\right)}\right| & \nu=3k+2\\ \left|\dfrac{\pi\nu\left(F^{\mathrm{I}}_{\Phi.\nu}-F^{\mathrm{II}}_{\Phi.\nu}\right)}{4\left(I_1N_1+I_1N_2+I_{\mathrm{II}}N_3\right)}\right| & \nu=3k+1\\ 0 & \nu=3k\end{cases}\tag{19}$$

The amplitude of an MMF harmonic is proportional to its corresponding RMC value. If the RMC value of a certain MMF harmonic is zero, that harmonic does not exist in the resultant MMF.

D. SELECTION OF COIL-SIDE CONDUCTOR NUMBERS

As mentioned previously, the coil-side conductor numbers of UCNC and ECNC have to be selected carefully because they have a considerable influence on the MMF of the proposed winding.

In order to facilitate the design of the driving system, the currents of winding-I and winding-II should be close. Hence, the winding factors of the working harmonic of the two sets of windings should also be close to balance the loads of the two sets of windings. To simplify the analysis, the winding factors of the working harmonic of the two sets of windings are considered to be equal. Thus, the conductors in series per phase of winding-I and winding-II are preferably equal, as expressed by

$$N_3=N_1+N_2\tag{20}$$

With the constraint of (20), Fig. 4 shows the variations in the different harmonics of the resultant MMF with N_1/N_2 (assuming $N_3=1$). The 5th harmonic must be included because it is the working harmonic. The 1st, 7th, and 17th harmonics are the main causes of high rotor loss in 12-slot/10-pole PMSM with the conventional FSCW so that they are also observed. It can be seen that the working harmonic exhibits minimal variation with N_1/N_2. Conversely, the 1st harmonic is quite sensitive to N_1/N_2 and is almost eliminated when N_1/N_2 is approximately 1.5. In terms of the 7th and 17th harmonics, regardless of the value of N_1/N_2, their amplitudes are always quite small.

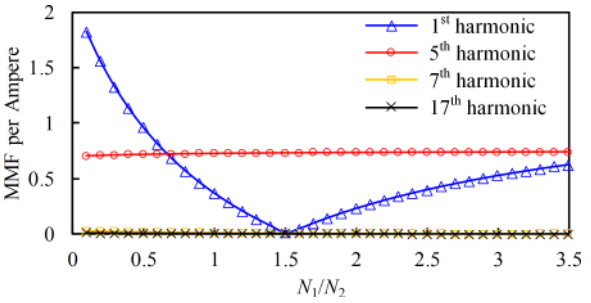

FIGURE 4. Variations of different MMF harmonics of the proposed winding with N_1/N_2.

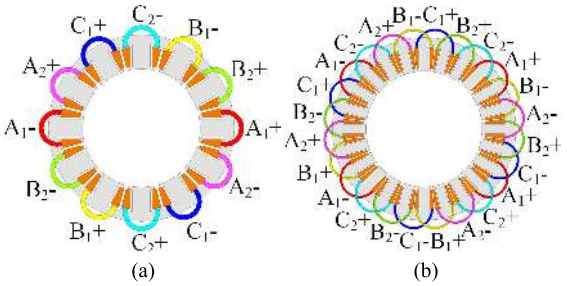

FIGURE 5. Configurations of two conventional windings. (a) DTP-FSCW. (b) TSP-FSW.

Naturally, the most appropriate ratio of N_1 to N_2 is approximately 1.5. Considering that the difference between N_1 and N_2 has to be one as mentioned previously, the coil-side conductor numbers are selected as

$$N_1=3,\quad N_2=2,\quad N_3=5\tag{21}$$

Now, the specific values of the winding factors and the RMCs of the proposed winding can be calculated, as tabulated in Table 3. For comparison, 12-slot/10-pole DTP-FSCW and 24-slot/10-pole TSP-FSW are also included in Table 3 and their configurations are illustrated in Fig. 5. The TSP-FSW is connected to be a DTP winding for a fair comparison. It should be clarified that the winding factors of both winding-I and winding-II of the proposal are given in Table 3 because

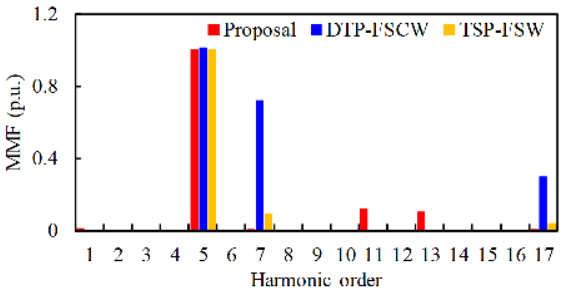

FIGURE 6. MMF harmonics of the three compared windings.

TABLE 3. Winding factors and RMCs of three windings.

	Proposal			DTP-FSCW		TSP-FSW	
v	$k_{w,v}^{I}$	$k_{w,v}^{II}$	RMC	$k_{w,v}$	RMC	$k_{w,v}$	RMC
1	0.254	0.259	0.0026	0.259	0	0.205	0
2	0	0	0	0	0	0	0
3	0.6	0.707	0	0.707	0	0.271	0
4	0	0	0	0	0	0	0
5	0.946	0.966	0.956	0.966	0.966	0.958	0.958
6	0	0	0	0	0	0	0
7	0.946	0.966	0.0097	0.966	0.966	0.126	0.126
8	0	0	0	0	0	0	0
9	0.6	0.707	0	0.707	0	0.653	0
10	0	0	0	0	0	0	0
11	0.254	0.259	0.256	0.259	0	0.158	0
12	0	0	0	0	0	0	0
13	0.254	0.259	0.256	0.259	0	0.158	0
14	0	0	0	0	0	0	0
15	0.6	0.707	0	0.707	0	0.653	0
16	0	0	0	0	0	0	0
17	0.946	0.966	0.0097	0.966	0.966	0.126	0.126

of their different configurations. As shown in Table 3, the winding factors of the working harmonic of winding-I and winding-II in the proposed winding are unequal (0.946 and 0.966, respectively) but the difference between them is very small (2%), which basically satisfies the assumption of the equal winding factors of the working harmonic of winding-I and winding-II.

In terms of the resultant MMF, the MMF spectra of the three windings can be obtained according to the RMCs presented in Table 3, as shown in Fig. 6. It can be seen from Fig. 6 that the 1st MMF harmonic of the proposal is nearly removed. Moreover, the 7th and 17th MMF harmonics almost disappear in the proposal. Therefore, the MMF of the proposed winding will be quite sinusoidal. TSP-FSCW also performs well in reducing MMF harmonics due to its low 1st and 7th harmonics. However, TSP-FSW does not support stator modularization as the proposed winding. Suffering from high 7th and 17th MMF harmonics, DTP-FSCW exhibits the highest non-working MMF harmonic content among the three windings.

IV. SIMULATION

Three SPM machines (namely M-I, M-II and M-III) with the proposed winding, DTP-FSCW and TSP-FSW are employed to be analyzed and compared by FEM. Their main design parameters are tabulated in Table 4, and their cross-sections are illustrated in Fig. 7.

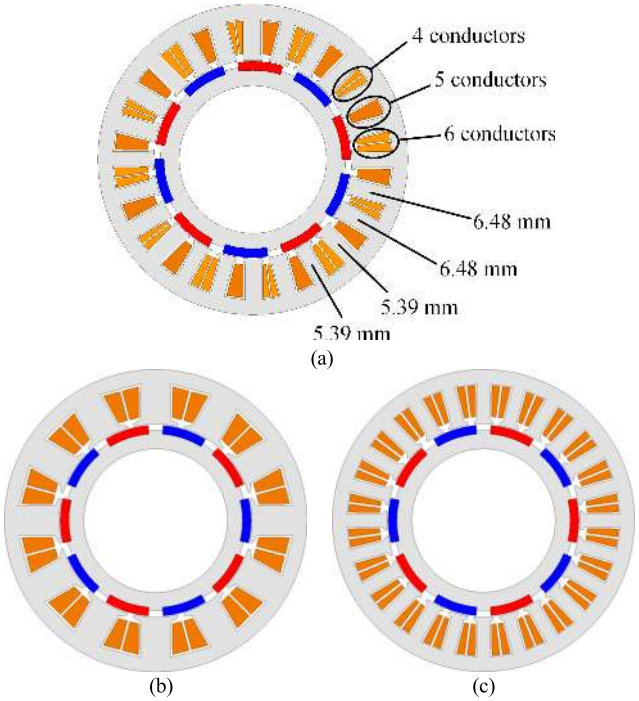

FIGURE 7. Cross-sections of the three compared machines. (a) M-I. (b) M-II. (c) M-III.

It should be noted that M-I has two different stator tooth widths (6.48 mm and 5.39 mm), as presented in Table 4. It is due to that three slot sizes have to be employed in M-I to fit the proposed winding configuration following the conductor numbers in (21), as illustrated in Fig. 7 (a). The two types of stator teeth with different widths are also indicated in Fig. 7 (a).

Instead of the commonly employed concept of number of *coil turns* in series per phase, the number of *conductors* in series per phase is employed here, which means that every conductor in series in a phase winding will be counted in the total. The main reason for this change is that the number of conductors on one coil-side differs from that on the other coil-side in a UCNC, which makes it difficult to define the number of coil turns of a UCNC.

The amplitudes of the rated phase currents of the three machines are set to be equivalent (50 A in RMS value), as presented in Table 4. It should be emphasized that winding-I and winding-II of the proposed winding have the same amplitudes of the phase currents. The rated phase current is relatively high due to the relatively low number of conductors in series. In fact, the number of conductors in series of the proposed winding can be a multiple of 20 by forming several groups of series-connected proposed windings in a machine. For convenient fabrication of the prototype, the number of groups of the proposed winding is only set to be one, which means the number of conductors in series is 20. Thus, the amplitude of the phase current should be increased to keep the electric load. However, it does not affect the validity of the evaluation and comparison of the three machines. In order to evaluate the influence of the end-winding length on copper loss, the

TABLE 4. Parameters of the three compared machines.

Parameters	M-I	M-II	M-III
Stator slot number	24	12	24
Pole number		10	
Stator outer diameter (mm)		122	
Stator inner diameter (mm)		78	
Slot opening width (mm)	2.5	2.59	2.5
Stator tooth width (mm)	6.48 & 5.39	12.04	5.1
Air-gap length (mm)		0.5	
PM height (mm)		3.5	
Pole arc coefficient		0.75	
Active axial length (mm)		40	
Number of conductors in series per phase		20	
Parallel branches	1	1	2
Core material		35CS250	
PM material		N42SH	
RMS rated phase current (A)		50	
Rated speed (rpm)		2400	

cross-section areas of the conductors of the three machines are designed to make the rated current densities of the three machines equal (3.9 A/mm^2). The output torque and power of the three machines are the performances to be examined, which will be calculated in the subsequent part of this section to evaluate the torque-producing capabilities of the three windings with the same electric load.

A. NO-LOAD BACK EMF

The no-load back EMF waves of M-I, M-II and M-III are calculated at the rated speed of 2400 rpm, as presented in Fig. 8. In addition, the harmonics of these on-load back EMF waves are shown in Fig. 9. It can be seen from Fig. 9 that the working harmonic of the no-load back EMFs of M-II is slightly higher than those of M-I and M-II because the DTP-FSCW exhibits the highest winding factor of the working harmonic among the three windings, as presented in Table 3. The no-load back EMFs of M-I with the proposed winding is unique among those of the three compared machines. It can be seen from Fig. 8 (a) that the no-load back EMF of winding-II in M-I lags behind that of winding-I by 90 electric degrees, which is consistent with the MMF analysis presented by (8) and (16). Moreover, the no-load back EMF wave of winding-I in M-I slightly differs from that of winding-II, as confirmed by their spectra shown in Fig. 9. This difference is caused by the different winding factors of winding-I and winding-II, as shown in Table 3.

B. COGGING TORQUE

The cogging torque waves of the three machines in the range of 60 mechanical degrees are shown in Fig. 10. It is obvious that M-II exhibits a much higher peak-to-peak value of the cogging torque than M-I and M-III because of its smallest least common multiple of slot number and pole number among the three machines.

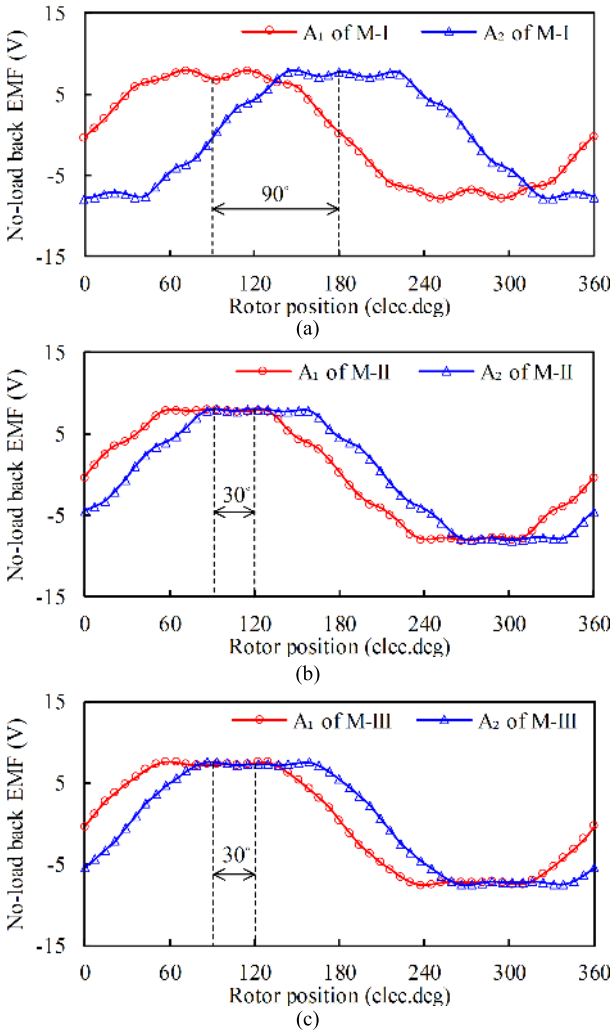

FIGURE 8. No-load back EMF waves. (a) M-I. (b) M-II. (c) M-III.

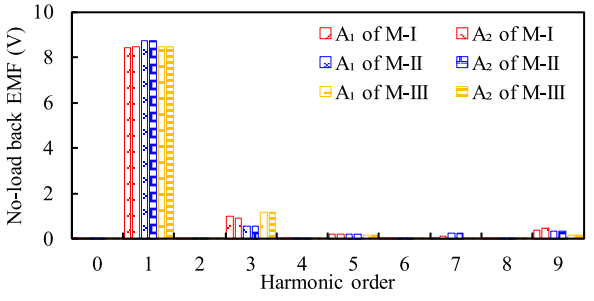

FIGURE 9. Harmonics of no-load back EMF waves.

It can also be seen from Fig. 10 that the cogging torque waves of M-I and M-III are quite similar since they have the same numbers of slots and poles. Nevertheless, subtle differences between the cogging torques of M-I and M-III can be observed. It is due to the employment of different stator tooth widths in M-I, as described in Fig. 7 (a), which causes different flux densities in the stator teeth. Thus, the minimum number of periods of the stator structure of M-I is six, which causes the difference between the cogging torques of M-I and M-III.

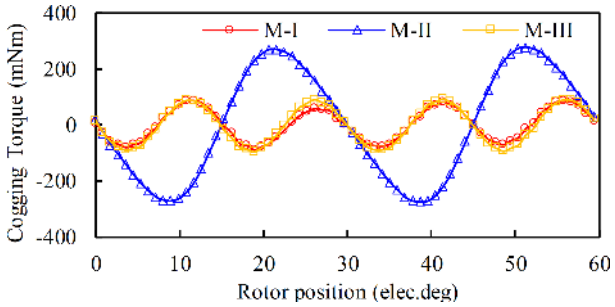

FIGURE 10. Cogging torque waves.

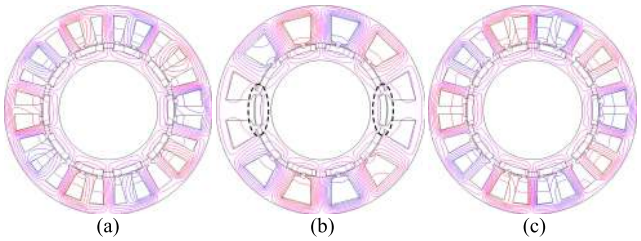

FIGURE 11. Armature reaction fields. (a) M-I. (b) M-II. (c) M-III.

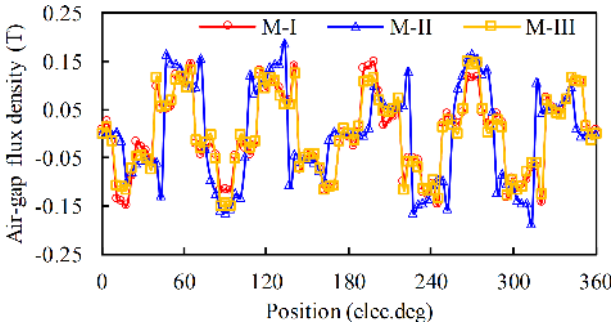

FIGURE 12. Air-gap flux density waves of armature reaction fields.

C. ARMATURE REACTION FIELD

The armature reaction fields of the three machines are computed by the frozen permeability method, as shown in Fig. 11. Moreover, the air-gap flux density waves of the armature reaction fields and their harmonics are presented in Fig. 12 and Fig. 13, respectively.

As observed in Fig. 11, the periodicities of the air-gap armature reaction fields of M-I and M-III are apparent. The periodicities are attributed to the low non-working harmonics of the air-gap flux density waves of the armature reaction fields in M-I and M-III as indicated in Fig. 13. Conversely, the air-gap armature reaction field of M-II is distorted within the areas marked by the dashed circles in Fig. 11 (b). The magnetic field distortion is mainly caused by the higher 7^{th} and 17^{th} harmonics in the air-gap flux density wave of the armature reaction field in M-II, as shown in Fig. 13.

By comparing Fig. 13 with Fig. 6, the correctness of the MMF analysis of the proposed winding can be verified. It can be seen from Fig. 13 that the 1^{st}, 7^{th} and 17^{th} harmonics of the armature reaction field of M-I are extremely low, which is in agreement with the MMF harmonic distribution of the

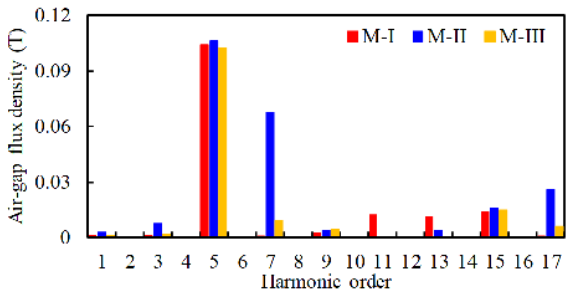

FIGURE 13. Harmonics of the air-gap flux densities of armature reaction fields.

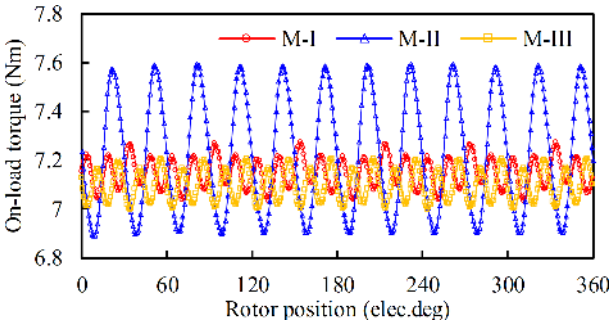

FIGURE 14. On-load torque waves.

proposed winding shown in Fig. 6. Overall, the spectra of the air-gap flux densities of the armature reaction fields presented in Fig. 13 are consistent with the MMF spectra presented in Fig. 6. However, there are some differences between the harmonic distributions in Fig. 6 and Fig. 13, especially in the 3^{rd} and 15^{th} harmonics. These differences are mainly caused by the magnetic modulation effect of the bulges on the rotor core between PM poles for accurate assembly of PMs.

D. ON-LOAD TORQUE

Fig. 14 presents the on-load torque waves of the three machines within one electric period of the working harmonic. Moreover, the average torques and torque ripples of the three machines are tabulated in Table 5. All the three machines are supplied with sinusoidal rated currents with the control strategy of $i_d = 0$ (i_d denotes the d-axis current). It can be seen from Table 5 that the average torques of M-I and M-III are close (7.144 Nm and 7.11 Nm, respectively) and both of them are slightly lower than that of M-II (7.231 Nm) due to the highest winding factor of the working harmonic of the DTP-FSCW. However, M-II has the highest torque ripple (9.74%) among the three machines because of its high peak-to-peak value of cogging torque, as shown in Fig. 10. The torque ripple of M-I (3.35%) is higher than that of M-II (2.91%) because the winding currents enlarge the difference between the flux densities in the stator teeth with different widths in M-I, which enhances the cogging effect of the stator of M-I.

E. LOSS AND EFFICIENCY

The losses of the three compared machines supplied with the rated sinusoidal currents are calculated at a speed of

TABLE 5. On-load torque performance.

	M-I	M-II	M-III
Average torque (Nm)	7.144	7.231	7.11
Torque ripple	3.35%	9.74%	2.91%

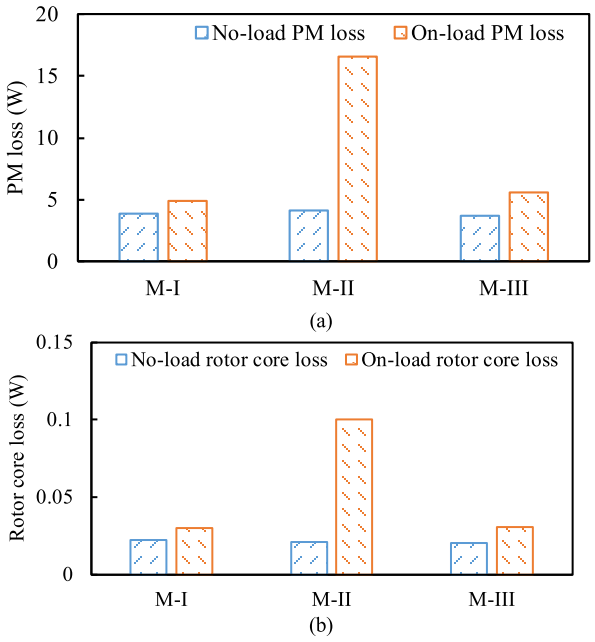

FIGURE 15. Rotor losses of the three compared machines. (a) PM losses. (b) Rotor core losses.

2400 rpm. Since one of the main purposes of the proposed winding is to reduce rotor loss, the rotor losses of the three machines are compared emphatically in Fig. 15. In order to evaluate the influences of the three windings on rotor loss more accurately, the no-load rotor losses of the three machines are designed to be almost equal.

It can be seen from Fig. 15 that M-I exhibits the lowest rotor loss among the three machines, as expected. The difference between the no-load and the on-load PM losses of M-I is very small, which indicates that the contribution of the armature reaction field generated by the proposed winding to rotor loss is extremely small owing to the low non-working harmonic content. The rotor loss of M-III is also small, which is only slightly higher than that of M-I. Conversely, the rotor loss of M-II is much higher than that of M-I and M-III (more than three times), which is mainly caused by the high 7^{th} and 17^{th} harmonics of the armature reaction field in M-II.

In addition to the rotor losses, the stator core losses and the copper losses of the three machines are also calculated. The influence of the end-winding on the copper loss is considered by calculating the end-winding length according to the method in [31]. The conductor lengths, including the end-windings of the three machines are presented in Fig. 16. It should be pointed out that the end-winding length of M-I with the proposed winding is obtained by weighted averaging due to the different numbers of coil-side conductors. As shown in

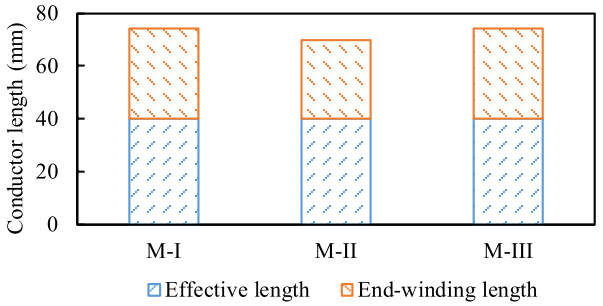

FIGURE 16. Conductor lengths of the three compared machines.

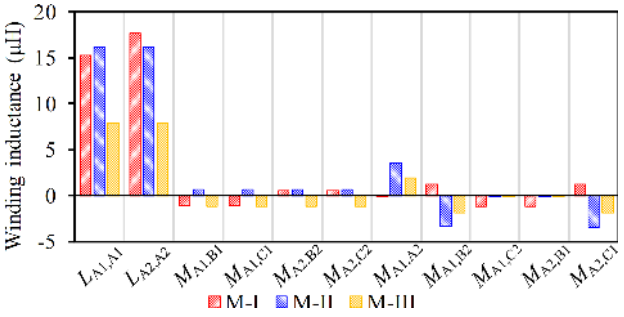

FIGURE 17. Winding inductances of the three compared machines.

Fig. 16, the end-winding length of M-I is 15% higher than that of M-II with FSCW because of the overlapped coils. The end-winding lengths of M-I and M-III are almost equal. The copper losses of the three machines will be proportional to their conductor lengths since their current densities are designed to be equal, as stated previously.

The losses in different parts and the efficiency of the three machines are tabulated in Table 6. The output powers of the three machines are calculated according to their average torque and speed. It can be seen from Table 6 that although M-I exhibits higher copper loss than that of M-II due to the overlapped coils, it still exhibits higher efficiency than M-II due to its lower PM loss.

F. FAULT TOLERANCE

Since the proposed winding is an overlapped winding, it is necessary to evaluate its fault tolerance. Low mutual inductance is helpful to improve the fault tolerance of the machine because it can prevent faults from spreading to healthy phases by magnetic coupling, which is referred to as magnetic insulation. Fig. 17 presents the winding inductances of the three compared machines. The maximum ratio of mutual inductance to self-inductance in M-I, M-II, and M-III is $M_{A1,B2}/L_{A1,A1}$ (8.25%), $M_{A1,A2}/L_{A1,A1}$ (21.61%), and $M_{A1,A2}/L_{A1,A1}$ (23.93%), respectively. Overall, the magnetic insulation among the phases in M-I is not perfect but it is passable among the three compared machines.

It can be noted that the mutual inductance between phase A_1 and phase A_2 of M-I is extremely low despite their overlapped coils. It can be explained by considering the main circuit of the magnetic field generated by phase A_2, as illustrated

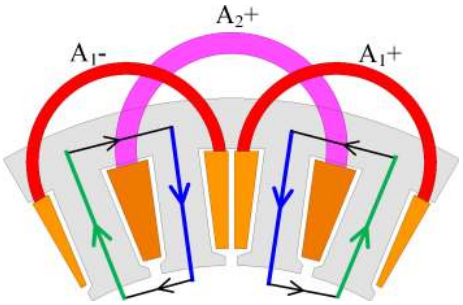

FIGURE 18. Main magnetic circuit of the armature reaction field of phase A_2 of M-I.

TABLE 6. Loss and efficiency.

	M-I	M-II	M-III
PM loss (W)	4.87	16.54	5.59
Rotor core loss (W)	0.03	0.1	0.03
Stator core loss (W)	24.5	23.92	25.4
Copper loss (W)	29.84	28.03	29.91
Output power (W)	1795.48	1817.35	1786.94
Efficiency	96.7%	96.23%	96.6%

in Fig. 18. It is obvious that the net coupling magnetic flux between phase A_1 and phase A_2 is almost zero because the magnetic fluxes indicated by the blue and the green arrows in Fig. 18 are in opposite directions.

The winding self-inductances of M-III are lower than those of M-I and M-II. The main causes are: (1) The number of coils per phase in M-III is relatively large (four); (2) The coils within a single phase of M-III are not adjacent to each other. The two characteristics of the winding configuration disperse the magnetic field generated by the phase winding in M-III, which makes the flux lines penetrate the air-gap more frequently, thereby increasing the encountered reluctance. Therefore, the self-inductance of the phase winding in M-III is decreased.

G. VOLTAGE BALANCE BETWEEN WINDING-I AND WINDING-II

It can noted from Fig. 17 the self-inductances of winding-I and winding-II in the proposed winding are different. Hence, it is necessary to survey the voltage balance of the two sets of windings. Fig. 19 (a) shows the on-load winding voltages of M-I in the rated working condition. In order to highlight the influence of the armature reaction on voltage balance, the winding voltages in the overloaded condition (four times the rated current) are also calculated, as shown in Fig. 19 (b). It can be seen from Fig. 19 that regardless of the working condition, the voltages of winding-I and winding-II are almost balanced. It should be emphasized that the amplitudes of the currents fed in the two sets of windings are always equal. Therefore, winding-I and winding-II in M-I are balanced in the current and voltage.

The reason for the voltage balance between winding-I and winding-II can be explained by considering the mutual inductances. It should be pointed out that the mutual inductances between the two sets of windings (such as $M_{A1\text{-}B2}$) do not

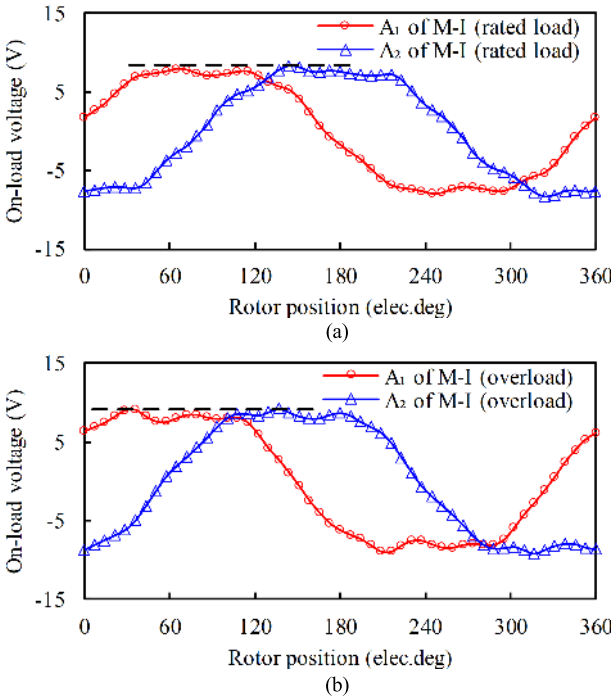

FIGURE 19. On-load winding voltages of M-I. (a) Rated load. (b) Overload (four times the rated current).

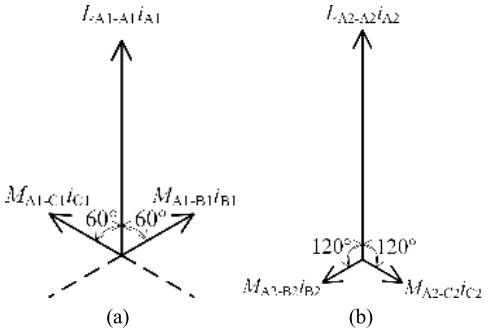

FIGURE 20. Illustration of the influence of mutual inductances on voltage balance. (a) Winding-I. (b) Winding-II.

need to be considered since the field coupling between the two sets of windings is mutual, which means that they have no influence on the voltage balance. It can be noted from Fig. 17 that the self-inductance of phase A_1 is about 13.48% lower than that of phase A_2. However, the mutual inductances within winding-I ($M_{A1\text{-}B1}$ and $M_{A1\text{-}C1}$) are negative. It means that voltage components in phase A_1 induced by phase B_1 and phase C_1 can increase the resultant voltage of phase A_1, which is illustrated by the phasor diagram shown in Fig. 20 (a). Conversely, the magnetic coupling among phase A_2, phase B_2 and phase C_2 will reduce the resultant voltage of phase A_2 because $M_{A2\text{-}B2}$ and $M_{A2\text{-}C2}$ are positive. The voltage reduction in phase A_2 is illustrated in Fig. 20 (b). Therefore, the difference between the voltages of phase A_1 and phase A_2 due to their different self-inductances is narrowed.

V. EXPERIMENT

A prototype of M-I was fabricated and tested to verity the theoretical analysis and FEM simulations. The photographs

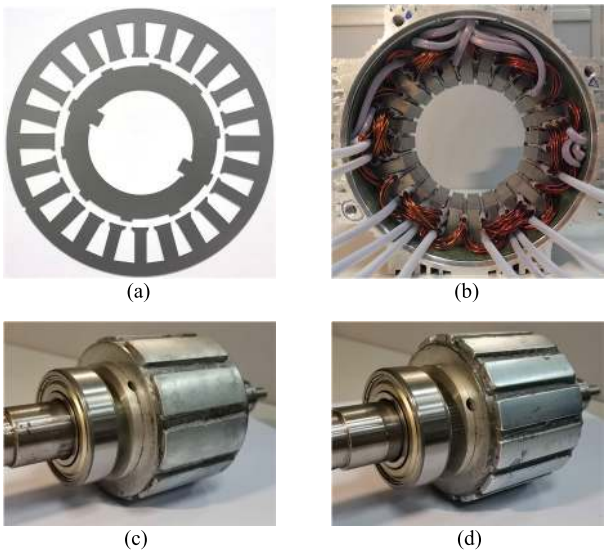

FIGURE 21. Photographs of the prototype. (a) Laminations. (b) Stator. (c) 10-pole rotor. (d) 14-pole rotor.

of the prototype are presented in Fig. 21. The slot space factor of the prototype is relatively low due to the limitation of the fabricating silks in such a small prototype, which reduces the cross-section area of the conductor. However, it does not affect the validity of the verification of the MMF analysis by the prototype since the winding configuration remains unchanged. This problem will not happen to a large direct-drive machine, for which the proposed winding is mainly designed. It is due to that the fully open slot with rectangular shape and the conductor with rectangular cross-section will be used in a large direct-drive machine, which will facilitate the filling of the stator slots. It should be noted that an extra rotor with 14 poles was fabricated to indirectly prove the MMF analysis of the proposed winding. The proof method will be described below.

The prototype was measured by a machine testing system, as shown in Fig. 22. The rated power of the load/traction machine is 5.5 kW and it can support a test at a speed up to 8,000 rpm. The employed torque senor has a measuring range of 0 Nm – 10 Nm. The relative linearity deviation and the relative tolerance of the sensitivity of the employed torque sensor are $< \pm 0.05\%$ F.S. and $\pm 0.1\%$ F.S., which are enough for the test since the torque ripple is about 3.35% according to the FEM result. The inverters support vector control and the control strategy of $i_d = 0$ was employed in the experiment.

A. NO-LOAD BACK EMF

The no-load back EMF waves generated by the 10-pole rotor and the 14-pole rotor at a speed of 2400 rpm are presented in Fig. 23. As shown in Fig. 23 (a), the measured no-load back EMFs excited by the 10-pole rotor show good agreement with the simulated results. Because of the difficulty in measuring the air-gap flux density, a 14-pole rotor is introduced to indirectly verify the MMF analysis by observing the phase relation between the no-load back EMFs of winding-I and

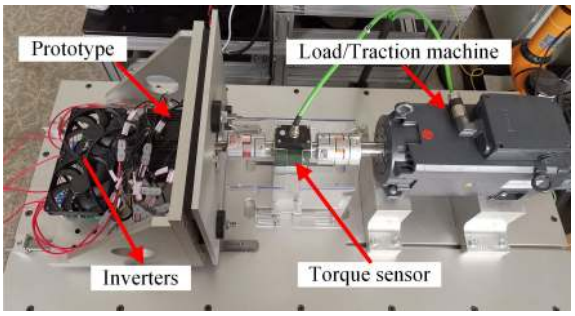

FIGURE 22. Machine traction testing system.

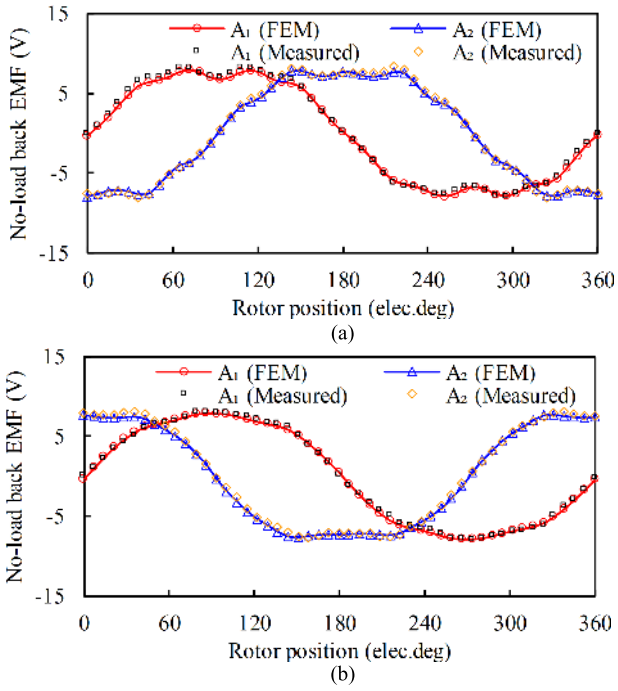

FIGURE 23. No-load back EMF waves of the prototype. (a) Using 10-pole rotor. (b) Using 14-pole rotor.

winding-II. According to (8) and (16). When a 14-pole rotor is employed, the no-load back EMF (excited by the 7th harmonic) of winding-II should be 90 degrees *ahead* of that of winding-I, which differs from the phase relation when a 10-pole rotor is employed. The simulation and the experiment results corroborate this theoretical prediction, as shown in Fig. 23 (b). For a clear comparison, the rotating direction of the 14-pole rotor is set to be opposite to that of the 10-pole rotor to ensure that the phase sequences of the no-load back EMFs generated by the two rotors are the same.

The agreement between the amplitude of the measured back EMF and that of the 2D FEM result can be explained by the influence of temperature on the performance of the PM material. The employed remanence of the PM material in the FEM simulation is 1.24 T (at 60°). However, the experiment was carried out in the environment with the temperature of 5° - 10°. Moreover, the duration of the experiment (including on-load condition) is short, which means that the PM temperature did not increase substantially. Therefore, the remanence

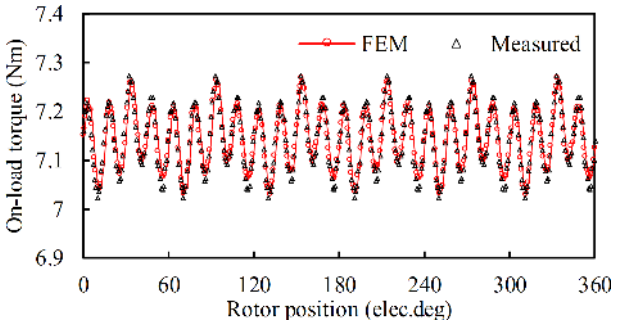

FIGURE 24. On-load torques of the prototype.

of the PM material during the experiment is estimated to be 1.33 T, which compensates for the loss of the back EMF due to the end effect.

B. ON-LOAD TORQUE

Fig. 24 shows the simulated and the measured on-load torques of the prototype fed with the rated phase current. It can be seen that the difference between the simulated torque and the measured torque is acceptable. The measured output torque is approximately 7.13 Nm, which is slightly lower than the simulated result (7.144 Nm). According to the measured output torque, the output power of the prototype can be calculated as approximately 1791.96 W.

VI. CONCLUSION

From the theoretical analysis, simulations and experiments, some key findings can be summarized:

1) The proposed winding allows the stator to be modularized. The stator of each cell machine (24-slot/10-pole) equipped with the proposed winding can be divided into six identical parts.
2) The proposed winding exhibits lower non-working MMF harmonic content than the conventional 12-slot/10-pole DTP-FSCW and 24-slot/10-pole TSP-FSW.
3) The PMSM with the proposed winding exhibits lower rotor loss than PMSMs with the conventional FSCW and TSP-FSW.
4) The freedom to choose the number of conductors in series per phase of the proposed winding is relatively weakened because of the adoption of UCNCs.

REFERENCES

[1] D.-J. Bang, H. Polinder, G. Shrestha, and J. A. Ferreira, "Promising direct-drive generator system for large wind turbines," *EPE J.*, vol. 18, no. 3, pp. 7–13, Sep. 2008.
[2] E. Fornasiero, L. Alberti, N. Bianchi, and S. Bolognani, "Considerations on selecting fractional-slot nonoverlapped coil windings," *IEEE Trans. Ind. Appl.*, vol. 49, no. 3, pp. 1316–1324, May/Jun. 2013.
[3] A. M. El-Refaie, "Fractional-slot concentrated-windings synchronous permanent magnet machines: Opportunities and challenges," *IEEE Trans. Ind. Electron.*, vol. 57, no. 1, pp. 107–121, Jan. 2010.
[4] N. Bianchi, S. Bolognani, M. D. Pre, and G. Grezzani, "Design considerations for fractional-slot winding configurations of synchronous machines," *IEEE Trans. Ind. Appl.*, vol. 42, no. 4, pp. 997–1006, Jul./Aug. 2006.
[5] H. Jussila, P. Salminen, M. Niemela, and J. Pyrhonen, "Guidelines for designing concentrated winding fractional slot permanent magnet machines," in *Proc. Int. Conf. Power Eng., Energy Electr. Drives*, Setubal, Portugal, Apr. 2007, pp. 191–194.
[6] N. Bianchi, M. D. Pre, L. Alberti, and E. Fornasiero, "Theory and design of fractional-slot PM machines," in *Proc. Conf. Rec. IEEE IAS Annu. Meeting*, New Orleans, LA, USA, Sep. 2007, p. 195.
[7] N. Bianchi and M. D. Pre, "Use of the star of slots in designing fractional-slot single-layer synchronous motors," *IEE Proc.-Electr. Power Appl.*, vol. 153, no. 3, pp. 459–466, 2006.
[8] D. A. Stone, P. H. Mellor, D. Howe, and K. Atallah, "Rotor loss in permanent-magnet brushless AC machines," *IEEE Trans. Ind. Appl.*, vol. 36, no. 6, pp. 1612–1618, Nov./Dec. 2000.
[9] N. Bianchi, S. Bolognani, and E. Fornasiero, "An overview of rotor losses determination in three-phase fractional-slot PM machines," *IEEE Trans. Ind. Appl.*, vol. 46, no. 6, pp. 2338–2345, Nov./Dec. 2010.
[10] N. Bianchi and E. Fornasiero, "Impact of MMF space harmonic on rotor losses in fractional-slot permanent-magnet machines," *IEEE Trans. Energy Convers.*, vol. 24, no. 2, pp. 323–328, Jun. 2009.
[11] E. Fornasiero, N. Bianchi, and S. Bolognani, "Slot harmonic impact on rotor losses in fractional-slot permanent-magnet machines," *IEEE Trans. Ind. Electron.*, vol. 59, no. 6, pp. 2557–2564, Jun. 2012.
[12] G. Dajaku and D. Gerling, "A novel 12-teeth/10-poles PM machine with flux barriers in stator yoke," in *Proc. 20th Int. Conf. Electr. Mach.*, Marseille, France, Sep. 2012, pp. 36–40.
[13] G. Dajaku, W. Xie, and D. Gerling, "Reduction of low space harmonics for the fractional slot concentrated windings using a novel stator design," *IEEE Trans. Magn.*, vol. 50, no. 5, pp. 1–12, May 2014.
[14] G. Dajaku and D. Gerling, "Low costs and high-efficiency electric machines," in *Proc. 2nd Int. Electr. Drives Prod. Conf. (EDPC)*, Nuremberg, Germany, Oct. 2012, pp. 1–7.
[15] Y. Wang, R. Qu, L. Wu, H. Fang, and D. Li, "Reduction of sub-harmonic effect on the fractional slot concentrated winding interior PM machines by using spoke-type magnets," in *Proc. IEEE Int. Electr. Mach. Drives Conf. (IEMDC)*, Coeur d'Alene, ID, USA, May 2015, pp. 1858–1863.
[16] L. Alberti, E. Fornasiero, and N. Bianchi, "Impact of the rotor yoke geometry on rotor losses in permanent-magnet machines," *IEEE Trans. Ind. Appl.*, vol. 48, no. 1, pp. 98–105, Jan./Feb. 2012.
[17] G. Choi and T. M. Jahns, "Reduction of eddy-current losses in fractional-slot concentrated-winding synchronous PM machines," *IEEE Trans. Magn.*, vol. 52, no. 7, pp. 1–4, Jul. 2016.
[18] L. Wu, R. Qu, and D. Li, "Reduction of rotor eddy-current losses for surface PM machines with fractional slot concentrated windings and retaining sleeve," *IEEE Trans. Magn.*, vol. 50, no. 11, pp. 1–4, Nov. 2014.
[19] A. S. Abdel-Khalik, S. Ahmed, and A. M. Massoud, "Low space harmonics cancelation in double-layer fractional slot winding using dual multi-phase winding," *IEEE Trans. Magn.*, vol. 51, no. 5, pp. 1–10, May 2015.
[20] L. Alberti and N. Bianchi, "Theory and design of fractional-slot multilayer windings," in *Proc. Energy Convers. Congr. Expo.*, Phoenix, AZ, USA, Sep. 2011, pp. 3112–3119.
[21] M. V. Cistelecan, F. J. T. E. Ferreira, and M. Popescu, "Three phase tooth-concentrated multiple-layer fractional windings with low space harmonic content," in *Proc. IEEE Energy Convers. Congr. Expo.*, Atlanta, GA, USA, Sep. 2010, pp. 1399–1405.
[22] P. B. Reddy, A. M. EL-Refaie, and K.-K. Huh, "Effect of number of layers on performance of fractional-slot concentrated-windings interior permanent magnet machines," *IEEE Trans. Power Electron.*, vol. 30, no. 4, pp. 2205–2218, Apr. 2015.
[23] A. Sun, J. Li, R. Qu, and D. Li, "Effect of multilayer windings on rotor losses of interior permanent magnet generator with fractional-slot concentrated-windings," *IEEE Trans. Magn.*, vol. 50, no. 11, pp. 1–4, Nov. 2014.
[24] G. Dajaku, "Elektrische maschine," German Patent 102 008 057 349 B3, Jul. 15, 2010.
[25] G. Dajaku and D. Gerling, "Eddy current loss minimization in rotor magnets of PM machines using high-efficiency 12-teeth/10-slots winding topology," in *Proc. Int. Conf. Electr. Mach. Syst.*, Beijing, China, Aug. 2011, pp. 1–6.
[26] J. Wang, K. Atallah, Z. Q. Zhu, and D. Howe, "Modular three-phase permanent-magnet brushless machines for in-wheel applications," *IEEE Trans. Veh. Technol.*, vol. 57, no. 5, pp. 2714–2720, Sep. 2008.
[27] P. B. Reddy, K.-K. Huh, and A. M. El-Refaie, "Generalized approach of stator shifting in interior permanent-magnet machines equipped with

fractional-slot concentrated windings," *IEEE Trans. Ind. Electron.*, vol. 61, no. 9, pp. 5035–5046, Sep. 2014.

[28] G. Dajaku and D. Gerling, "A novel 24-slots/10-poles winding topology for electric machines," in *Proc. IEEE Int. Electr. Mach. Drives Conf. (IEMDC)*, Niagara Falls, ON, Canada, May 2011, pp. 65–70.

[29] J. Wang, V. I. Patel, and W. Wang, "Fractional-slot permanent magnet brushless machines with low space harmonic contents," *IEEE Trans. Magn.*, vol. 50, no. 1, pp. 1–9, Jan. 2014.

[30] V. I. Patel, J. Wang, W. Wang, and X. Chen, "Six-phase fractional-slot-per-pole-per-phase permanent-magnet machines with low space harmonics for electric vehicle application," *IEEE Trans. Ind. Appl.*, vol. 50, no. 4, pp. 2554–2563, Jul. 2014.

[31] K. Wang, Z. Q. Zhu, and G. Ombach, "Synthesis of high performance fractional-slot permanent-magnet machines with coil-pitch of two slot-pitches," *IEEE Trans. Energy Convers.*, vol. 29, no. 3, pp. 758–770, Sep. 2014.

[32] A. S. Abdel-Khalik, S. Ahmed, and A. M. Massoud, "A six-phase 24-slot/10-Pole permanent-magnet machine with low space harmonics for electric vehicle applications," *IEEE Trans. Magn.*, vol. 52, no. 6, pp. 1–10, Jun. 2016.

[33] Y. Yue, L. Wu, and S. Jia, "Comparison of IPM machines with fractional-slot concentrated windings and coil-pitch of two slot-pitches windings for EV application," in *Proc. 21st Int. Conf. Electr. Mach. Syst. (ICEMS)*, Jeju, South Korea, Oct. 2018, pp. 275–279.

[34] M. Harke, "Design of fractional slot windings with coil span of two slots for use in six-phase synchronous machines," *J. Eng.*, vol. 2019, no. 17, pp. 4391–4395, Jun. 2019.

[35] M. Harke, "Fractional slot windings with a coil span of two slots and less content of low order harmonics," in *Proc. Int. Symp. Power Electron., Electr. Drives, Autom. Motion (SPEEDAM)*, Amalfi, Italy, Jun. 2018, pp. 1309–1314.

[36] H. Y. Sun and K. Wang, "Space harmonics elimination for fractional-slot windings with two-slot coil pitch," *IEEE Access*, vol. 7, pp. 106961–106972, 2019.

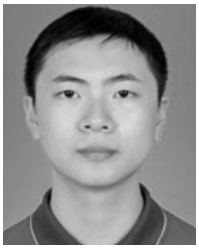

KEYI WANG received the B.Eng. degree from Southeast University, Nanjing, China, in 2014, where he is currently pursuing the Ph.D. degree in electrical engineering. His current research interests include the design of permanent magnet machines and winding theory.

HEYUN LIN (Senior Member, IEEE) received the B.S., M.S., and Ph.D. degrees in electrical engineering from the Nanjing University of Aeronautics and Astronautics, Nanjing, China, in 1985, 1989, and 1992, respectively.

From 1992 to 1994, he was a Postdoctoral Fellow with Southeast University, Nanjing. In 1994, he joined the School of Electrical Engineering, Southeast University as an Associate Professor and became a Full Professor, in 2000. He has authored more than 200 technical articles and the holder of 60 patents. His main research is related to the design, analysis and control of permanent magnet motors, intelligent electrical apparatus, and electromagnetic field numerical analysis. He is a Fellow of IET, a member of the Electrical Motor and Apparatus Committee of Jiangsu Province, and a Senior Member of the China Society of Electrical Engineering and China Electrotechnical Society.